Check for updates

Small

NANO · MICRO small
www.small-journal.com

RESEARCH ARTICLE

High-Strength Degradable Transparent Bio-Electronics Enabled by Confined Crystallization in Aligned Nanofibers for AI-Assisted Motion Sensors

Chu Pan[1] | Xueyi Li[2] | Chuanfeng Wang[1,3] | Juan Li[1] | Wangjie Xu[1] | Biyao Huang[1] | Xuhang Lu[1] | Jiashun Wen[1] | Weiqing Yang[4] | Jun Lu[1]

[1]School of Chemistry, Southwest Jiaotong University, Chengdu, Sichuan, China | [2]Guangdong Institute of Smart Education, Jinan University, Guangzhou, Guangdong, China | [3]Key Laboratory of Advanced Technologies of Materials, School of Materials Science and Engineering, Ministry of Education, Southwest Jiaotong University, Chengdu, Sichuan, China | [4]Research Institute of Frontier Science, Southwest Jiaotong University, Chengdu, Sichuan, China

Correspondence: Weiqing Yang (wqyang@swjtu.edu.cn) | Jun Lu (junluprc@hotmail.com)

Received: 4 August 2025 | **Revised:** 31 December 2025 | **Accepted:** 6 January 2026

Keywords: machine learning | motion monitoring | poly (3-hydroxybutyrate-3-hydroxyvalerate) | silver nanowire | transparent conductive film

ABSTRACT

The severe environmental impact of conventional plastic electronics necessitates next-generation wearable devices simultaneously embodying high performance, flexibility, and sustainability. Herein, we propose a 1D nano-confined high-pressure crystallization strategy to create highly-crystalline, yet highly-transparent bio-based fiber films to meet these requirements. The bacterial copolymer poly (3-hydroxybutyrate-3-hydroxyvalerate) (PHBV)-based electrospun fibrous film, with 1D-confined oriented crystallites in the aligned nanofibers, can be transformed from opaque to transparent by heating and pressurizing and maintains its fiber morphology. The resulting film demonstrates outstanding flexibility, high optical transmittance, and significantly enhanced mechanical properties. Using this transparent fiber film as the substrate, a transparent conductive film (TCF) is produced by mechanical interlocking with silver nanowires (AgNWs), demonstrating superior performance in comprehensive metrics compared to the state-of-the-art TCFs. Critically, this TCF achieves high-fidelity capture of electromyography and electrocardiography (ECG) signals, comparable to commercial gel electrodes, while showing enhanced signal stability on sweat-soaked skin. As a proof-of-concept, a motion monitoring system is designed integrating AgNWs/PHBV-based ECG acquisition, Bluetooth transmission, and a multilayer perceptron-based classification model. Leveraging machine learning, it accurately classifies athletes' physical activity states and provides personalized training recommendations. This study may offer a new way of utilizing biological materials and inspire the development of next-generation sustainable electronics.

1 | Introduction

Growing interest is being directed toward wearable and mobile technologies that enhance the functionalities of smart wearables, e-skins, and human-machine interactions [1–12]. Simultaneously, the need for flexible, transparent, low-cost, and easily manufactured devices is driving the emergence of plastic electronics [13–16]. Traditionally, the transparent substrates of devices, such as polyester (PET), polydimethylsiloxane (PDMS), and polyurethane (PU), are typically characterized by short lifespan and non-degradability, which inevitably poses a significant range of critical environmental and sustainability issues [17]. Annually, an estimated excess of 390 million tons of plastic are produced (Plastics Europe 2023) and will be discarded into natural environments, causing serious ecosystem problems [17]. Hence, there arises an imperative necessity to develop environmentally

© 2026 Wiley-VCH GmbH

friendly and sustainable transparent materials for fabricating green flexible electronics.

Biological materials are those materials produced by natural biological systems. Examples include silk fibroin [18], wood [19, 20], plant [21, 22], and other biomass [23, 24]. Biological materials have attracted much interest owing to their benefits of very low cost, non-toxicity, renewability, and excellent biodegradability [18–25]. To be more precise, researchers reported transparent films made by simple mechanical pressing and drying, using wood and cellulose nanofibers from which lignin and hemicellulose were removed [19, 25]. Moreover, Cheng et al. produced a transparent wood by bleaching the wood and infiltrating it with epoxy resin to match the refractive index [20]. These transparent films preserved the original alignment of cellulose nanofibers and nanostructures, and presented higher mechanical properties compared to the same materials cast by solutions [19]. However, the pretreatment of these materials consumes plenty of chemical solutions and energy, making it necessary to propose a simplified method.

Poly (3-hydroxybutyrate-3-hydroxyvalerate) (PHBV) is an ideal biodegradable material with high crystallinity and good mechanical properties [26]. Unlike synthetic petroleum-based plastics, PHBV copolymers can be produced by bacteria utilizing agricultural residues under mild conditions [27–30], which achieves cost savings and reduced carbon emissions. Also, modification enables PHBV to achieve a tunable degradation rate, which further improves its practicability [31]. Nevertheless, similar to a petroleum-based crystalline polymer, the brittleness and the opacity of the intrinsically highly crystalline PHBV hinder its extensive applications in flexible transparent electronics [26]. To address these problems, many methods have been proposed, such as blending and grafting [26, 32–34]. And grain engineering is a strategy to enhance the strength, dielectric or photoelectric properties, and transparency of materials by controlling the size or orientation of grains [35–39]. Moreover, electrospinning technology is a convenient method to manufacture functional composites [40–42]. 1D confined crystallization occurs when polymer chains crystallize within 1D nanochannels [43–45]. During electrospinning, the spatial confinement imposed by the nanofiber geometry restricts the crystal growth perpendicular to the fiber axis. Consequently, this confinement promotes the preferential crystal orientation along the direction of the nanofibers [43–45].

In this work, we develop a bacterial PHBV copolymer-based highly crystalline, yet highly transparent fibrous film by 1D nano-confined high-pressure crystallization. Under appropriate heating and pressurization conditions, the electrospun nanofiber film can be transformed from opaque to transparent while maintaining the fiber morphology. The resulting film demonstrates outstanding flexibility, high optical transmittance, and enhanced mechanical properties. Using the transparent fiber film as the substrate, we fabricate a transparent conductive film (TCF) by mechanical interlocking with silver nanowires (AgNWs) that exhibits high electrical conductivity and high mechanical stability. During exercise heart rate monitoring, the TCF-based wearable system performs comparably to the commercial gel electrode-based counterpart in acquiring electromyography (EMG) and electrocardiography (ECG) signals, while demonstrating superior signal stability on sweaty skin. As a proof of concept, a motion monitoring system is further designed by integrating AgNWs/PHBV-based ECG acquisition, Bluetooth transmission, and a classification model based on a multilayer perceptron (MLP). With the assistance of machine learning, the system can accurately classify athletes' physical activity states and provide personalized recommendations, showing significant potential for human motion monitoring and exercise optimization.

2 | Results and Discussion

2.1 | Design of Transparent Film with Fibrous Structure

The key to the design of a transparent film with fibrous structure is the preparation of oriented crystallites and aligned nanofibers (Figure 1a). The aligned nanofibers are prepared by electrospinning. Controlling the roller speed enables precise manipulation of nanofiber orientation, yielding highly aligned structures. And the nanocrystallites are grown under the constraint of aligned nanofibers, achieving preferred crystalline orientation. Initially, a significant amount of light loss occurs at the interface of the fibrous membrane (Figure 1b). After proper heating and pressing treatment, the fibrous membrane becomes transparent, and its strength is significantly increased (Figure 1c). In Figure 1d, the tensile strength and light transmittance of different films are compared. The transparent PHBV fibrous film shows outstanding properties among the degradable films [20, 46–55]. As a proof-of-concept, a motion monitoring system is designed, including EMG and ECG signals acquisition, and machine learning for human motion monitoring and exercise optimization (Figure 1e).

2.2 | Characterization of Random/Aligned Electrospun PHBV Fibrous Membranes and Transparent Hot-Pressed PHBV Film

Generally, the propagation of light in crystalline polymers is governed by birefringence, refractive index anisotropy, and scattering. These materials typically comprise ordered crystalline regions and disordered amorphous regions, resulting in anisotropic optical properties. Upon entering a crystalline domain, light may experience birefringence. Additionally, the refractive index contrast at the interface between crystalline and amorphous regions can cause reflection. When the crystal size exceeds the wavelength of visible light, Rayleigh scattering occurs. Larger crystal sizes or higher crystallinity lead to more pronounced scattering, which consequently reduces material transparency. Therefore, to achieve higher transparency, researchers controlled or refined the size and arrangement of spherulites [56–58]. Here, two different roller speeds (1000 and 4000 rpm) were used for electrospinning to investigate the effects on fiber orientation and internal nanocrystallite orientation. As presented in Figure 2a,b,e,f, the scanning electron microscopy (SEM) and corresponding statistical fiber diameter distribution reveal that the random electrospun PHBV fibers (R-ES-PHBV, fabricated at 1000 rpm) have a larger diameter and a more chaotic distribution than the aligned electrospun PHBV fibers (A-ES-PHBV, fabricated at 4000 rpm). The fast Fourier transform (FFT) images directly visualize the radial distribution of

16136829, 2026, 14, Downloaded from https://onlinelibrary.wiley.com/doi/10.1002/smll.202509404 by Jilin University, Wiley Online Library on [07/11/2026]. See the Terms and Conditions (https://onlinelibrary.wiley.com/terms-and-conditions) on Wiley Online Library for rules of use; OA articles are governed by the applicable Creative Commons License

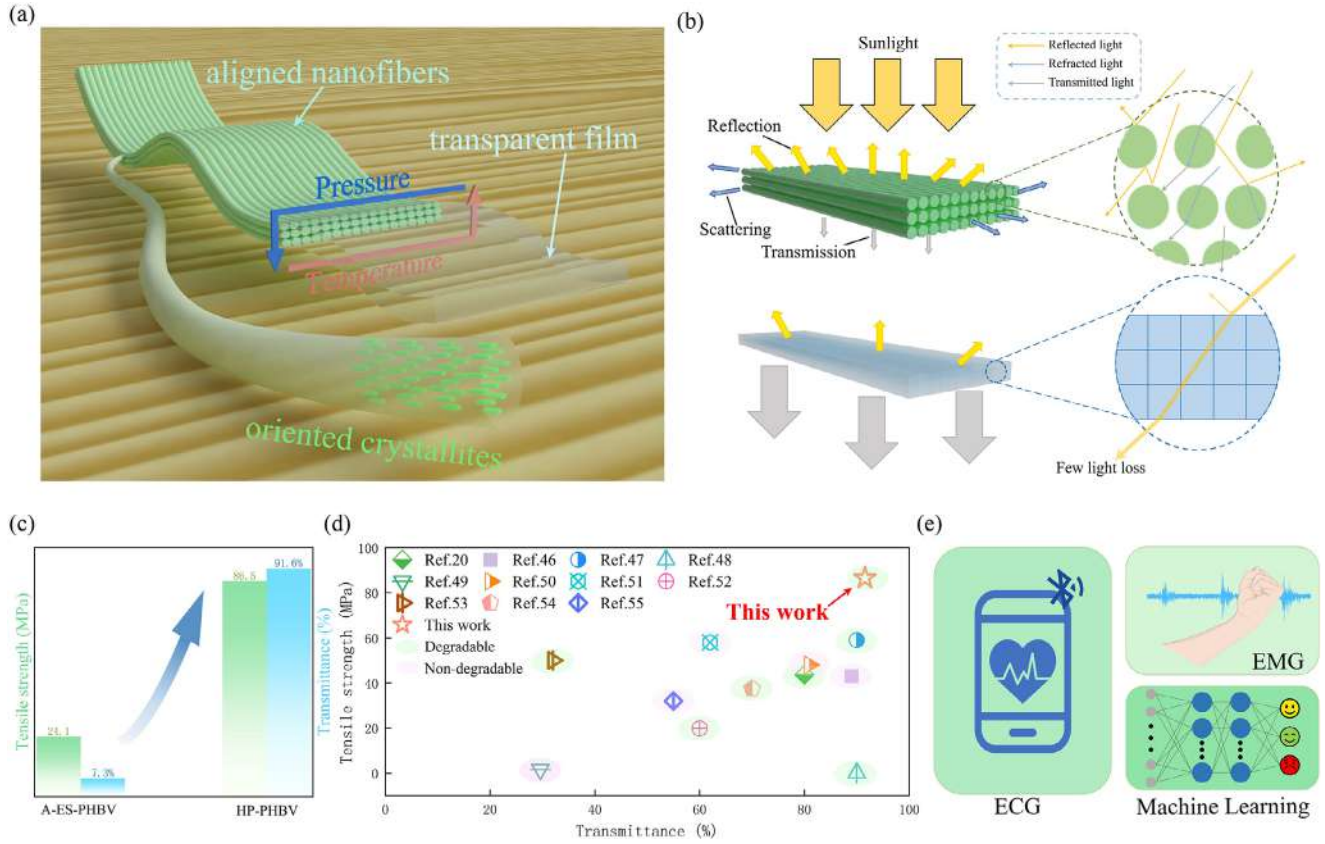


FIGURE 1 | Overview of transparent film with fibrous structure. (a) Schematic composition of transparent film with fibrous structure. (b) Schematic illustration of the mechanism of light propagation in fibrous membranes. (c) Increase in tensile strength and light transmittance after heating and pressing. (d) Values of tensile strength versus light transmittance for HP-PHBV compared with other reported materials. (e) Schematic illustration showing the motion monitoring system for EMG and ECG signals acquisition, human motion monitoring, and human motion recognition.

R-ES-PHBV and the uniaxial alignment of A-ES-PHBV (Figure 2c,g). Nanocrystallites orientation in the samples was further characterized through X-ray pole figures of the PHBV (020) crystal plane (Figure 2d,h). The polar density region can reveal the degree of orientation of samples [45, 59]. Compared with R-ES-PHBV, A-ES-PHBV has a stronger fiber texture with a maximum density value of 4.124, and has a more concentrated density distribution, confirming its higher degree of orientation. After heating and pressing, A-ES-PHBV transforms into transparent hot-pressed PHBV (HP-PHBV). As shown in Figure 2i, the fibers fit closely, which significantly reduces the interface between air and fiber. Meanwhile, the fibrous structure is maintained (Figure 2j,k), which significantly enhances the strength and flexibility of the film. In addition, owing to the hot-press and annealing process, HP-PHBV exhibits optimal orientation with a peak density value of 4.737, and its density distribution converges to a single point (Figure 2l).

2.3 | Optical and Mechanical Properties of HP-PHBV and Mechanism for the Transformation of Transparency

As shown in Figure 3a, the HP-PHBV fabrication process is simple and consumes little energy. First, A-ES-PHBV was fabricated by electrospinning under suitable conditions. Then the fibrous membrane was subjected to a pressure of 200 MPa at 120°C for 10 min. This was followed by annealing under maintained pressure at a cooling rate of −0.25°C/min for 4 h. Finally, the resulting HP-PHBV achieved high transparency, with a light transmittance of 91.6% at 550 nm (Figure 3b,c). For transparent films, haze provides a direct metric of forward scattering in the materials. As shown in Figure S1, the haze of HP-PHBV is comparatively low (5.9% at 550 nm), whereas R-ES-PHBV and A-ES-PHBV exhibit the very high haze values of 98.2% and 99.2%, respectively. This significant difference in haze indicates that the processing method substantially reduces light scattering in HP-PHBV. Figure 3d further demonstrates that HP-PHBV has a low optical haze; even when placed 10 cm above the blackboard, the white grid remains clearly visible. Due to the maintained microfiber structure, HP-PHBV can be easily bent even after being frozen in liquid nitrogen, exhibiting excellent flexibility (Figure 3e). The differential scanning calorimetry (DSC) results show that HP-PHBV has a melting temperature (T_m) of 179°C and a crystallinity (X_c) of 64.0%. These values are slightly higher than those of A-ES-PHBV (177°C and 63.0%, respectively) (Figure 3f). The increase can be attributed to the enhanced crystal perfection during high-pressure annealing, where the applied heat and pressure promote further structural ordering. Additionally, the tensile force exerted by the roller during processing significantly improves the polymer molecular chain orientation and crystallinity. Consequently, due to the absence of similar treatment conditions, R-ES-PHBV shows the lowest values (176°C and 57.1%, respectively). The X-ray diffraction (XRD) spectra reveal crystalline differences: β phase is

16136829, 2026, 14, Downloaded from https://onlinelibrary.wiley.com/doi/10.1002/smll.202509404 by Jilin University, Wiley Online Library on [07/11/2026]. See the Terms and Conditions (https://onlinelibrary.wiley.com/terms-and-conditions) on Wiley Online Library for rules of use; OA articles are governed by the applicable Creative Commons License

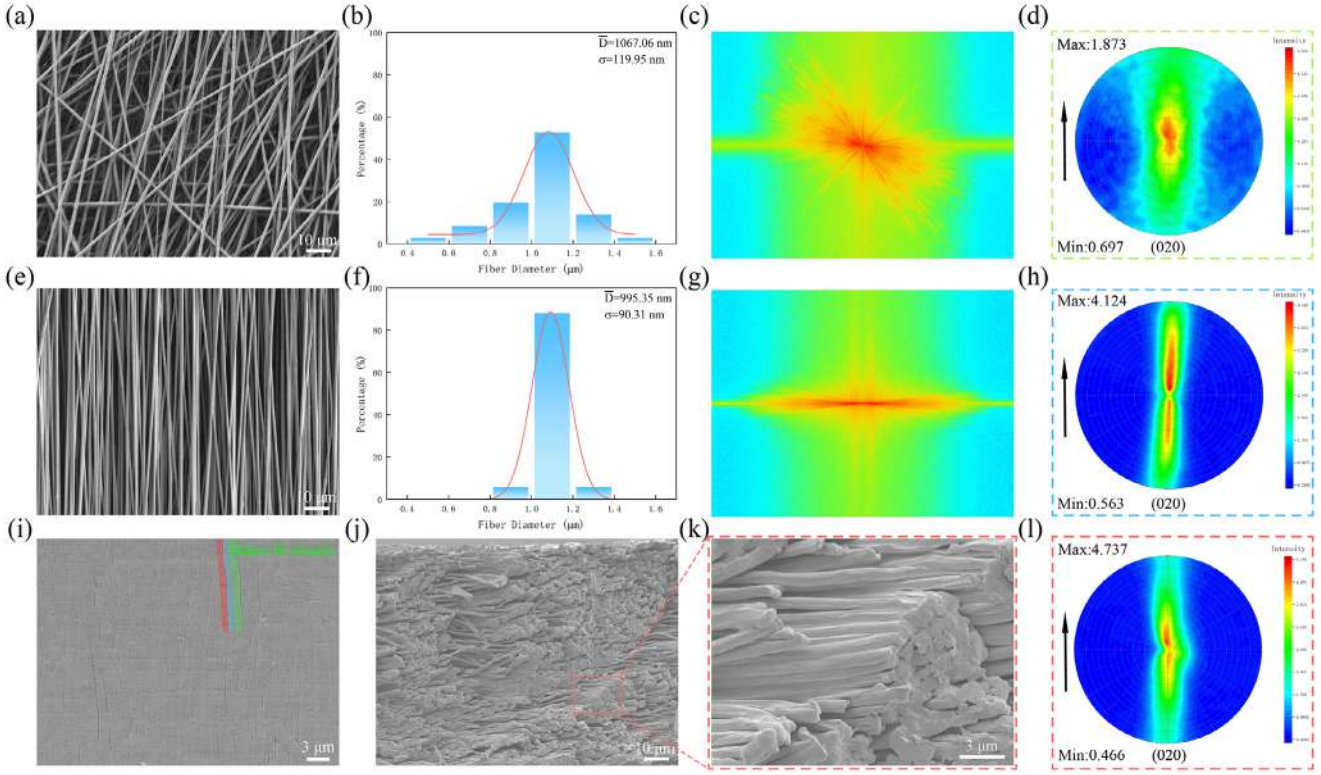


FIGURE 2 | Characterization of R-ES-PHBV, A-ES-PHBV, and HP-PHBV. (a) SEM image, (b) statistical diameter distribution, (c) FFT image derived from (a), and (d) X-ray pole figure of R-ES-PHBV. (e) SEM image, (f) statistical diameter distribution, (g) FFT image derived from (e), and (h) X-ray pole figure of A-ES-PHBV. (i) SEM image of surface, (j, k) SEM image of cross section, and (l) X-ray pole figure of HP-PHBV.

present in A-ES-PHBV. The β phase is formed during the drawing of high-speed electrospinning [60]. High temperature and high pressure cause the transition from β-phase to α-phase, leading to decreased β-phase intensity in HP-PHBV. Notably, the high X_c and fibrous structure endow HP-PHBV with excellent mechanical strength (Figure 3h).

Sunlight interaction with materials inherently involves absorption, reflection, and scattering phenomena. Absence of visible-light chromophores in PHBV enables low absorption; however, its fibrous membrane exhibits opaque whiteness owing to intense interfacial light scattering and reflection. As demonstrated above, the mechanism for the transformation to transparency can be summed up as the reduction of interfacial light scattering and reflection. ① The oriented nanocrystallites minimize the light scattering in the PHBV fiber. The average dimensions of nanocrystallites were calculated using Scherrer's formula [61]

$$D = \frac{K\lambda}{\beta\cos\theta} \tag{1}$$

where D is the dimension of crystallite, K is a shape constant, λ is the wavelength of X-rays, β is the full-width at half maxima of the diffraction line, and θ is the peak position or diffraction angle. Scherrer analysis applied to the (020) and (110) diffraction peaks indicated the crystallite sizes of 17.74 and 15.98 nm, respectively. It demonstrates that the D is smaller than the wavelength of visible light (λ_{vis}), and the light transmission through HP-PHBV is dominated by the Rayleigh scattering regime ($D \ll \lambda_{vis}$) [62]. In this case, the transmittance (T) of the film can be characterized by the analytical form of the Chandrasekhar radiative transfer equation, which is given as [63, 64]

$$T - \frac{1}{1 + \frac{3}{4}\rho\sigma_{sct}h} \tag{2}$$

where ρ is the density, h is the thickness of the HP-PHBV slab, and σ_{sct} is the scattering cross-section. In addition, the σ_{sct} is proportional to D^3. The formula above reveals that the transparency of HP-PHBV is significantly enhanced by reducing the dimension of crystallites (i.e., the smaller $\sigma_{sct} \propto D^3$, then the larger T) [62]. ② The compact fibrous structure reduces the air-fiber interface, leading to minimized light reflection and increased optical transmittance. The light reflection at an interface is governed by the refractive index contrast between the two constituent materials. It can be described by the Fresnel formula, which is defined as [65]

$$r = \left(\frac{n_F - n_A}{n_F + n_A}\right)^2 \tag{3}$$

where r is the reflective coefficient, and n_F and n_A are the refractive indices of the fiber and air, respectively. The r at the air-fiber interface is significantly higher than that at the compact fiber-fiber interface ($r \approx 0$). Consequently, the light reflection in HP-PHBV is markedly lower than that in A-ES-PHBV. In short, by fabricating nanofiber-confined oriented nanocrystallites and compacting the interface of aligned fibers, the interfacial light reflection and scattering are minimized, thus achieving high optical transparency of the fibrous membrane.

16136829, 2026, 14, Downloaded from https://onlinelibrary.wiley.com/doi/10.1002/smll.202509404 by Jilin University, Wiley Online Library on [07/11/2026]. See the Terms and Conditions (https://onlinelibrary.wiley.com/terms-and-conditions) on Wiley Online Library for rules of use; OA articles are governed by the applicable Creative Commons License

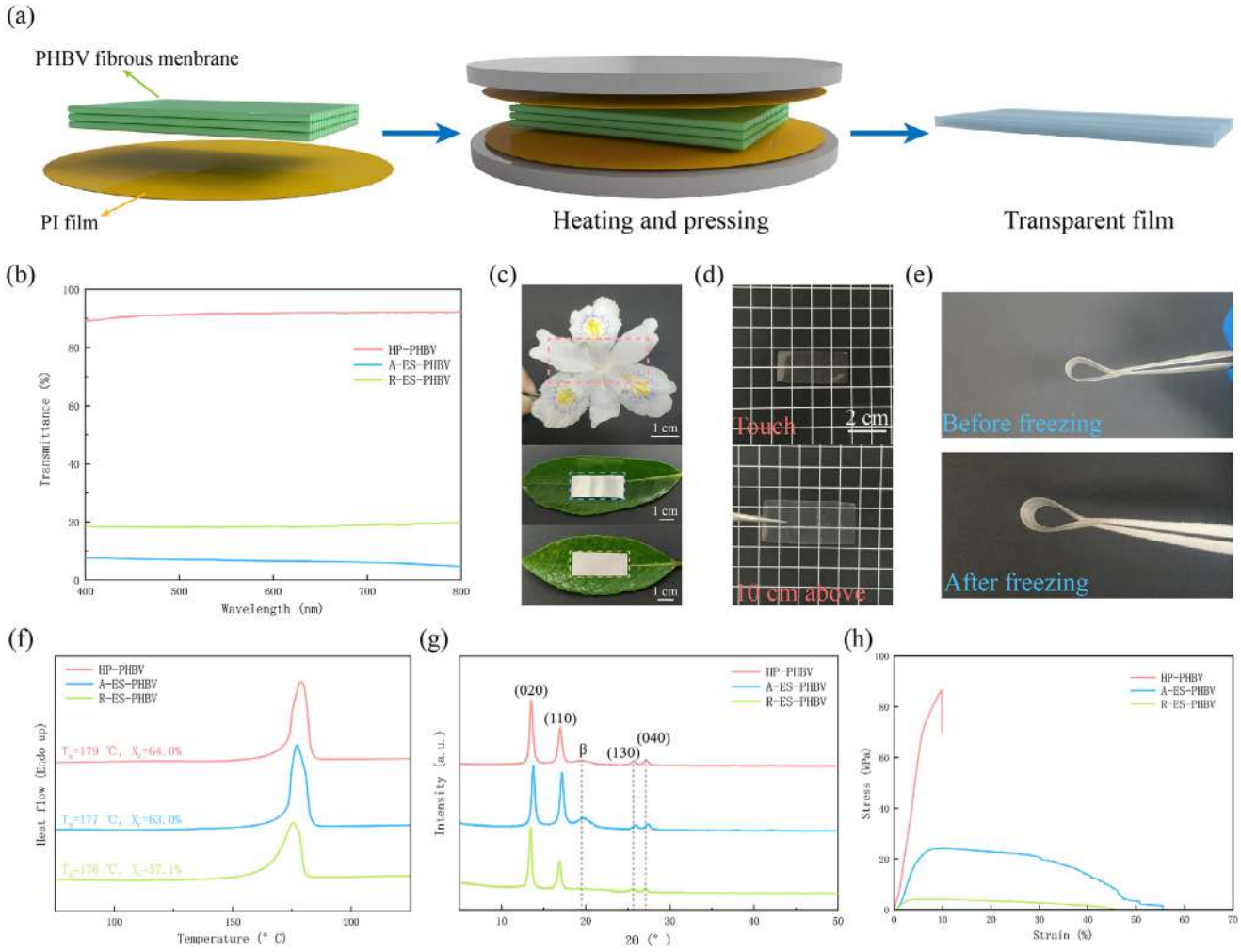


FIGURE 3 | Optical and mechanical properties of HP-PHBV. (a) Schematic illustration of HP-PHBV fabrication. (b) Transmittance of HP-PHBV, A-ES-PHBV, and R-ES-PHBV in visible light (400-800 nm). (c) Digital images of HP-PHBV (top), A-ES-PHBV (middle), and R-ES-PHBV (bottom). (d) HP-PHBV directly onto the board (top) and 10 cm above the board (bottom). (e) Digital images of HP-PHBV showing flexibility before/after freezing. (f) DSC, (g) XRD, and (h) tensile stress–strain curves of HP-PHBV, A-ES-PHBV, and R-ES-PHBV.

2.4 | Optical, Electrical, and Degradable Properties of AgNWs/PHBV

The fabrication process of AgNWs/PHBV is shown in Figure 4a. To ensure forming a continuous conductive network and achieving strong adhesion between AgNWs and fibers, the thin R-ES-PHBV was pretreated by plasma cleaning for 3 min with an RF power of 18 W in air [66]. After vacuum filtration, the AgNWs are uniformly distributed on the plasma-treated membrane that assists in forming conductive networks (Figure 4b,c; Figure S2). The electrospun PHBV fiber networks deposited on poly (ether-ether-ketone) (PEEK) film functioned to immobilize the AgNWs on the surface via mechanical interlocking (Figure S3). After heating and pressing, the final obtained AgNWs/PHBV presents a compact structure with a thickness of 40 μm (Figure 4d,e; Figure S4). The energy dispersive spectrometer (EDS) elemental mapping further confirms the homogeneous distribution of AgNWs (Figure S5). Increasing the amount of AgNWs reduces optical transmittance by intensifying light reflection and scattering (Figure 4f). Simultaneously, this increases the number of AgNW junction points to achieve lower sheet resistance (Figure 4g). At 60 μL AgNWs loading, AgNWs/PHBV achieves competitive performance: transmittance of 78.0% (at 550 nm) and sheet resistance of 30.5 Ω/sq, indicating excellent performance balancing for TCF. Using AgNWs/PHBV as a conducting wire, the light-emitting diode (LED) operates stably in the continuous bending state of AgNWs/PHBV (Figure 4h). Notably, the AgNWs/PHBV demonstrates excellent stability, with < 8% resistance change over 13,000 bending cycles (Figure 4i). Overall, the radar chart highlights the superior transmittance, sheet resistance, strength, long-term stability, and degradability of AgNWs/PHBV compared to other TCFs (Figure S6 and Table S1).

The degradation behavior is a key indicator of biodegradable materials. To evaluate the durability of AgNWs/PHBV in practical applications, in vitro hydrolysis and high-temperature (58°C) soil compost experiments were conducted. As shown in Figure S7, the in vitro hydrolysis and soil compost tests present entirely different results. After 2 months of in vitro hydrolytic degradation, the AgNWs/PHBV exhibited differential residual mass across pH environments (pH = 1, 7.2, and 12, respectively). Although showing the fastest degradation rate at pH = 12, it still

16136829, 2026, 14, Downloaded from https://onlinelibrary.wiley.com/doi/10.1002/smll.202509404 by Jilin University, Wiley Online Library on [07/11/2026]. See the Terms and Conditions (https://onlinelibrary.wiley.com/terms-and-conditions) on Wiley Online Library for rules of use; OA articles are governed by the applicable Creative Commons License

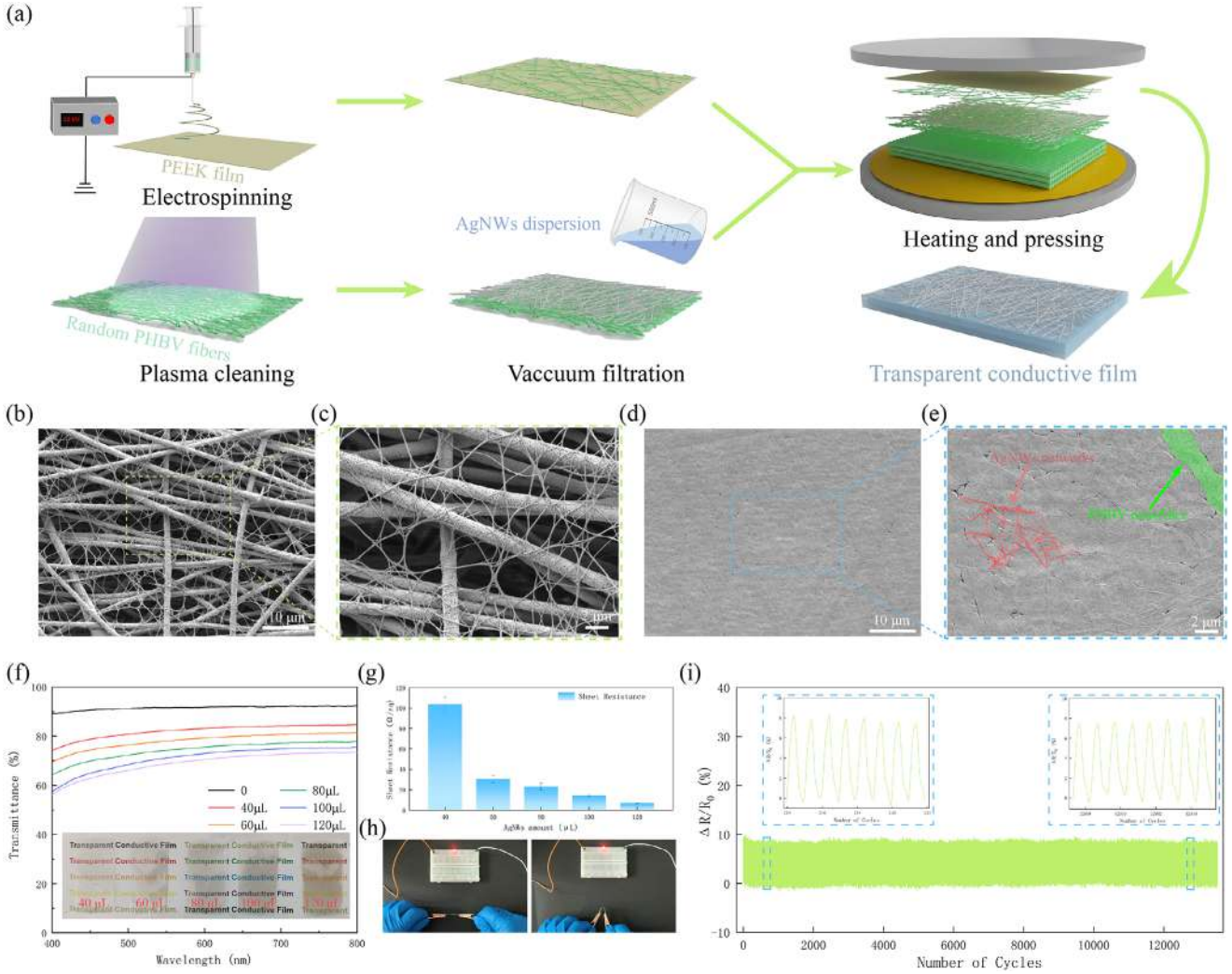


FIGURE 4 | Fabrication, micromorphology, and properties of AgNWs/PHBV. (a) Schematic illustration of AgNWs/PHBV fabrication. (b, c) SEM images of AgNWs/PHBV before heating and pressing. (d, e) SEM images of AgNWs/PHBV after heating and pressing. (f, g) Transmittance and sheet resistance of AgNWs/PHBV with different amounts of AgNWs; inset: digital images of corresponding films. (h) Electrical properties of AgNWs/PHBV during bending. (i) Resistance changes of AgNWs/PHBV during cyclic bending. The bending radius is 3 mm.

maintained > 95% mass. Solution-materials interactions loosened the compact surface, leading to the opaque region formation via interfacial delamination. In contrast, the AgNWs/PHBV underwent extremely rapid degradation in a high-temperature soil composting environment. Within 5 days, the film was basically degraded. The two completely different degradation behaviors enable flexible applications: the TCF remains stable when exposed to sweat during exercise (pH = 4.5–7.0) [67], while the discarded TCF can be degraded rapidly by soil composting. Thus, the PHBV-based TCFs show significant potential for sustainable electronics.

2.5 | Wearable System Integration and Human Motion Monitoring Assisted with Machine Learning

Traditionally, the commercial gel electrodes for motion monitoring are disposable, incurring high expenses for daily exercise recording. In this case, the durable and biocompatible AgNWs/PHBV conductive film presents a promising alternative. For EMG detection, the AgNWs/PHBV film was attached to the forearm of a volunteer to record the action potential generated by muscle fibers (Figure 5a). When the volunteer made different gestures, the EMG signals corresponding to each gesture were clearly observed (Figure 5b). The signals acquired by AgNWs/PHBV film exhibited higher noise than those from the commercial gel electrode, attributed to the triboelectric effect between the film and skin. Despite this, it presented a higher signal amplitude, indicating a superior recognition efficiency, while maintaining a signal-to-noise ratio (SNR) of around 15 dB (Figure 5c). To enable real-time heart rate monitoring, a wearable sensor (based on a Bluetooth acquisition module) was developed to capture high-fidelity ECG data (Figure 5d). It recorded clear characteristic ECG waveforms from a volunteer. Comparatively, the AgNWs/PHBV film exhibited a similar waveform morphology, but the signal amplitude was ~47.6% higher than that of the commercial gel electrode (Figure 5e). The clear visualization of the cardiac cycle revealed the distinguishable waveforms associated with heart rhythm: P-wave (atrial excitation), QRS complex (ventricular excitation), and T-wave (ventricular relaxation), as shown in

16136829, 2026, 14, Downloaded from https://onlinelibrary.wiley.com/doi/10.1002/smll.202509404 by Jilin University, Wiley Online Library on [07/11/2026]. See the Terms and Conditions (https://onlinelibrary.wiley.com/terms-and-conditions) on Wiley Online Library for rules of use; OA articles are governed by the applicable Creative Commons License

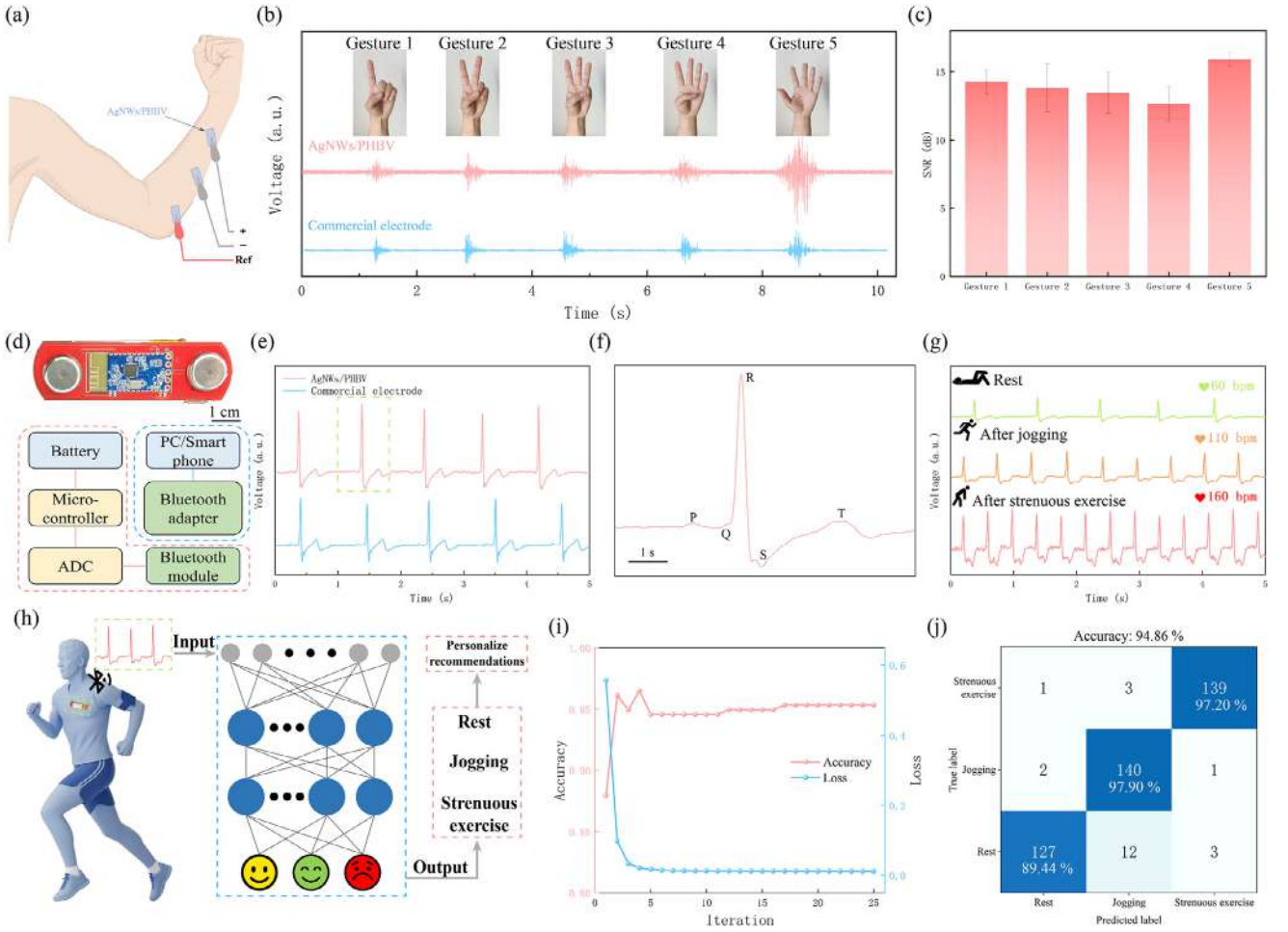


FIGURE 5 | Bioelectric detection of AgNWs/PHBV electrode and a machine learning assisted human motion monitoring system. (a) Schematic illustration of EMG detection. (b) EMG signals recorded by AgNWs/PHBV and commercial gel electrodes during repeated executions of gestures 1–5, and (c) corresponding SNR of EMG signals acquired by AgNWs/PHBV. (d) Schematic illustration of a wearable sensor system for ECG signal monitoring, including signal acquisition, processing, Bluetooth transmission, and applications programs. (e) ECG signals recorded by AgNWs/PHBV and commercial gel electrodes. (f) Typical cardiac waveform, showing high precision and rich features. (g) ECG signals were recorded during rest, after jogging, and after strenuous exercise. (h) Machine learning algorithm of MLP for human motion recognition. (i) Evaluation of the model accuracy in 25 iterations and the training process in fine-tuning. (j) Confusion map of the machine learning results for 3 categories.

Figure 5f. After varying intensity exercise, the AgNWs/PHBV film maintained high-fidelity ECG acquisition, whereas the commercial gel electrode exhibited signal degradation under sweaty conditions (Figure 5g and Figure S8). Furthermore, the AgNWs/PHBV film demonstrated excellent durability by maintaining high-fidelity ECG signals and exhibiting no visible degradation after 7 days of immersion in artificial sweat or exposure to UV radiation (Figure S9).

Heart rates during physical exercise vary within and between individuals. This complicates the assessment of exercise intensity. To provide personalized exercise recommendations, a human motion monitoring system was developed by integrating AgNWs/PHBV-based ECG acquisition, Bluetooth transmission, and a classification model based on a multilayer perceptron (MLP) (Figure 5h). Machine learning analysis of complex ECG patterns can detect subtle changes imperceptible to human eyes, thereby improving the assessment of physical activity. An optimized MLP architecture was developed to classify ECG signals across three physical activity states. The MLP model consisted of three fully connected hidden layers with ReLU activation and Adam optimizer (initial learning rate 0.001), implemented using PyTorch. A robust preprocessing pipeline, including outlier-resistant scaling and SMOTE-based oversampling, was employed to address signal variation and class imbalance. This pipeline facilitates effective feature learning from raw ECG time-series data, whereafter embedding these features into a high-dimensional space for accurate activity classification. 80% of the collected data was used for model training and 20% for testing to evaluate the algorithm's prediction accuracy. To mitigate overfitting, five-fold cross-validation was conducted across sessions, ensuring model generalization. The high-fidelity ECG signals obtained from the AgNWs/PHBV electrodes not only improved the overall data fidelity but also significantly enhanced the signal-to-noise ratio. High-quality signals reduce baseline drifts, motion artifacts, and other physiological or environmental interferences that typically degrade machine learning performance. By providing cleaner and more stable waveform characteristics, the AgNWs/PHBV electrodes enabled downstream machine learning algorithms to extract more discriminative temporal and

16136829, 2026, 14, Downloaded from https://onlinelibrary.wiley.com/doi/10.1002/smll.202509404 by Jilin University, Wiley Online Library on [07/11/2026]. See the Terms and Conditions (https://onlinelibrary.wiley.com/terms-and-conditions) on Wiley Online Library for rules of use; OA articles are governed by the applicable Creative Commons License

morphological features. This reduction in noise-induced feature distortion effectively mitigated overfitting and enhanced the robustness of the learned representations. Attributed to high-fidelity ECG signals, the model showed accelerated loss convergence within 25 iterations. To prevent overfitting, dropout layers were introduced during fine-tuning. The MLP model demonstrated a decoding accuracy of 95.33% during training (Figure 5i). With 94.86% overall accuracy, the model accurately classified physical activity states, achieving 97.90% for jogging and 97.20% for strenuous exercise (Figure 5j). The exercise intensity was evaluated in conjunction with the exercise time, and a personalized recommendation was provided accordingly. Leveraging the datasets collected by the integrated system based on AgNWs/PHBV, the MLP model demonstrates significant potential for human motion monitoring and exercise optimization.

3 | Conclusion

In summary, we have successfully developed a bacterial copolymer PHBV-based highly crystalline, yet highly transparent fibrous film by a 1D nano-confined high-pressure crystallization process. The electrospun fibrous film, with 1D-confined oriented crystallites in the aligned nanofibers, could be transformed from opaque to transparent by heating and pressurizing and maintained its fiber morphology. The resulting film exhibited outstanding flexibility, high optical transmittance, and significantly enhanced tensile strength. Using this transparent fiber film as a substrate, a TCF was further fabricated by mechanical interlocking with AgNWs. Compared to state-of-the-art TCFs, the AgNWs/PHBV-based TCF demonstrated superior performance in comprehensive metrics, including light transmittance, sheet resistance, strength, long-term stability, and degradability. Critically, this TCF achieved a high-fidelity capture of EMG and ECG signals, comparable to commercial gel electrodes, while showing enhanced signal stability on sweat-soaked skin. As a proof-of-concept, a motion monitoring system was designed by integrating AgNWs/PHBV-based ECG acquisition, Bluetooth transmission, and an MLP-based classification model. Leveraging machine learning, the system could accurately classify athletes' physical activity states and could provide personalized recommendations, showing great potential in human motion monitoring and exercise optimization. We anticipate that the facile strategy adopted in this work will offer a new way of utilizing biological materials and will inspire the development of next-generation sustainable electronics.

4 | Experimental Section

The detailed description of materials, experimental process, and characterizations is presented in the Supporting Information.

4.1 | Ethical Approval and Informed Consent

The individual involved in the sensing test was exclusively limited to the first author himself (Chu Pan). The AgNWs/PHBV bioelectrode-based wearable system is non-invasive and harmless. The approval from the relevant ethics committee is not required for this study. All included participants in this experiment gave their oral and written informed consent.

4.2 | Statistical Analysis

Sample sizes (n) for statistical analysis were as follows: fiber diameter ($n = 35$), sheet resistance ($n = 8$), and SNR ($n = 3$). Statistical analysis and graphing were carried out using OriginPro 2024 (OriginLab, USA).

Acknowledgements

This work was financially supported by National Natural Science Foundation of China (No. 52073237). The authors would like to thank the Analysis and Testing Center of Southwest Jiaotong University.

Conflicts of Interest

The authors declare no conflicts of interest.

Data Availability Statement

The data that support the findings of this study are available from the corresponding author upon reasonable request.

References

1. X. Zhao, Y. Zhou, W. Kwak, et al., "A Reconfigurable and Conformal Liquid Sensor for Ambulatory Cardiac Monitoring," *Nature Communications* 15, no. 1 (2024): 8492.

2. X. Zhao, Y. Zhou, A. Li, et al., "A Self-Filtering Liquid Acoustic Sensor for Voice Recognition," *Nature Electronics* 7, no. 10 (2024): 924–932.

3. Y. Zhou, X. Zhao, J. Xu, et al., "Giant Magnetoelastic Effect in Soft Systems for Bioelectronics," *Nature Materials* 20, no. 12 (2021): 1670–1676.

4. J. Yin, S. Wang, T. Tat, and J. Chen, "Motion Artefact Management for Soft Bioelectronics," *Nat Rev Bioeng* 2, no. 7 (2024): 541–558.

5. X. Zhao, Y. Zhou, Y. Song, et al., "Permanent Fluidic Magnets for Liquid Bioelectronics," *Nature Materials* 23, no. 5 (2024): 703–710.

6. A. Libanori, G. Chen, X. Zhao, Y. Zhou, and J. Chen, "Smart Textiles for Personalized Healthcare," *Nature Electronics* 5, no. 3 (2022): 142–156.

7. X. Zhao, Y. Zhou, J. Xu, et al., "Soft Fibers With Magnetoelasticity for Wearable Electronics," *Nature Communications* 12, no. 1 (2021): 6755.

8. S. Kim, G. Lee, C. Jeon, et al., "Bimetallic Nanocatalysts Immobilized in Nanoporous Hydrogels for Long-Term Robust Continuous Glucose Monitoring of Smart Contact Lens," *Advanced Materials* 34, no. 18 (2022): 2110536.

9. B. Zhang, J. Li, J. Zhou, et al., "3D Liquid Diode for Soft, Integrated Permeable Electronics," *Nature* 628 (2024): 84–92.

10. K. Zheng, Y. Tong, S. Zhang, et al., "Flexible Bicolorimetric Polyacrylamide/Chitosan Hydrogels for Smart Real-Time Monitoring and Promotion of Wound Healing," *Advanced Functional Materials* 31, no. 34: 2102599, https://doi.org/10.1002/adfm.202102599.

11. F. Chen, Q. Zhuang, Y. Ding, et al., "Wet-Adaptive Electronic Skin," *Advanced Materials* 35, no. 49 (2023): 2305630.

12. Y. Li, Z. Qiu, H. Kan, et al., "A Human-Computer Interaction Strategy for an FPGA Platform Boosted Integrated "Perception-Memory" System Based on Electronic Tattoos and Memristors," *Advanced Science* 11, no. 39 (2024): 2402582.

13. T. S. Dinh Le, J. An, Y. Huang, et al., "Ultrasensitive Anti-Interference Voice Recognition by Bio-Inspired Skin-Attachable Self-Cleaning

16136829, 2026, 14, Downloaded from https://onlinelibrary.wiley.com/doi/10.1002/smll.202509404 by Jilin University, Wiley Online Library on [07/11/2026]. See the Terms and Conditions (https://onlinelibrary.wiley.com/terms-and-conditions) on Wiley Online Library for rules of use; OA articles are governed by the applicable Creative Commons License

Acoustic Sensors," *ACS Nano* 13, no. 11 (2019): 13293–13303, https://doi.org/10.1021/acsnano.9b06354.

14. J. An, T. D. Le, C. H. J. Lim, et al., "Single-Step Selective Laser Writing of Flexible Photodetectors for Wearable Optoelectronics," *Advanced Science* 5, no. 8 (2018): 1800496, https://doi.org/10.1002/advs.201800496.

15. S. Cho, S. Kang, A. Pandya, et al., "Large-Area Cross-Aligned Silver Nanowire Electrodes for Flexible, Transparent, and Force-Sensitive Mechanochromic Touch Screens," *ACS Nano* 11, no. 4 (2017): 4346–4357, https://doi.org/10.1021/acsnano.7b01714.

16. D. Zhong, C. Wu, Y. Jiang, et al., "High-Speed and Large-Scale Intrinsically Stretchable Integrated Circuits," *Nature* 627, no. 8003 (2024): 313–320.

17. V. Dhaka, S. Singh, A. G. Anil, et al., "Toxicity and Remediation of Polyethylene Terephthalate Plastics. A Review," *Environmental Chemistry Letters* 20, no. 3 (2022): 1777–1800.

18. S. Li, Y. Zhang, X. Liang, et al., "Humidity-Sensitive Chemoelectric Flexible Sensors Based on Metal-Air Redox Reaction for Health Management," *Nature Communications* 13, no. 1 (2022): 5416.

19. Q. Fu, Y. Chen, and M. Sorieul, "Wood-Based Flexible Electronics," *ACS Nano* 14, no. 3 (2020): 3528–3538, https://doi.org/10.1021/acsnano.9b09817.

20. M. Cheng, M. Ying, R. Zhao, et al., "Transparent and Flexible Electromagnetic Interference Shielding Materials by Constructing Sandwich AgNW@MXene/Wood Composites," *ACS Nano* 16 (2022): 16996–17007.

21. Y. Wan, Z. Qiu, J. Huang, et al., "Natural Plant Materials as Dielectric Layer for Highly Sensitive Flexible Electronic Skin," *Small* 14 (2018): 1801657, https://doi.org/10.1002/smll.201801657.

22. V. Sharma, A. Koivikko, K. Yiannacou, K. Lahtonen, and V. Sariola, "Flexible Biodegradable Transparent Heaters Based on Fractal-Like Leaf Skeletons," *npj Flex Electron* 4, no. 1 (2020): 27.

23. H. Abral, J. Ariksa, M. Mahardika, et al., "Transparent and Antimicrobial Cellulose Film From Ginger Nanofiber," *Food Hydrocolloids* 98 (2020): 105266, https://doi.org/10.1016/j.foodhyd.2019.105266.

24. Y. B. Kwon, S. Cho, D. H. Min, and Y. K. Kim, "Durable Silver Nanowire Transparent Electrodes Enabled by Biorenewable Nanocoating Using Chitin and Cellulose Nanofibers for Flexible Electronics," *Nanoscale Horiz* 9, no. 11 (2024): 2051–2059.

25. M. Nogi, S. Iwamoto, A. N. Nakagaito, and H. Yano, "Optically Transparent Nanofiber Paper," *Advanced Materials* 21, no. 16 (2009): 1595–1598, https://doi.org/10.1002/adma.200803174.

26. A. Gupta, L. Lolic, and T. H. Mekonnen, "Reactive Extrusion of Highly Filled, Compatibilized, and Sustainable PHBV/PBAT—Hemp Residue Biocomposite," *Composites Part A: Applied Science and Manufacturing* 156 (2022): 106885, https://doi.org/10.1016/j.compositesa.2022.106885.

27. C. Hierro-Iglesias, C. O. Fatokun, A. Chimphango, et al., "Process Integration for Efficient Conversion of Cassava Peel Waste Into Polyhydroxyalkanoates," *Journal of Environmental Chemical Engineering* 12, no. 1 (2024): 111815.

28. C. M. Laumeyer, J. Zimmer, and H. Steinmetz, "From Fruit Juice Wastewater to Biopolymer—How the Mixed Microbial Culture and PHA Content Develop Over Time," *Chemical Engineering Journal* 503 (2025): 158314, https://doi.org/10.1016/j.cej.2024.158314.

29. S. K. Bhatia, R. Gurav, T.-R. Choi, et al., "Bioconversion of Plant Biomass Hydrolysate Into Bioplastic (Polyhydroxyalkanoates) Using Ralstonia Eutropha 5119," *Bioresource Technology* 271 (2019): 306–315, https://doi.org/10.1016/j.biortech.2018.09.122.

30. M. Kumar, R. Rathour, R. Singh, et al., "Bacterial Polyhydroxyalkanoates: Opportunities, Challenges, and Prospects," *Journal of Cleaner Production* 263 (2020): 121500.

31. J. Zhu, Y. Chen, H.-Y. Yu, et al., "Comprehensive Insight Into Degradation Mechanism of Green Biopolyester Nanocomposites Using Functionalized Cellulose Nanocrystals," *ACS Sustainable Chemistry & Engineering* 7, no. 18 (2019): 15537–15547, https://doi.org/10.1021/acssuschemeng.9b03291.

32. R. D. Bairwan, L. Sukeksi, H. P. S. A. Khalil, et al., "Poly(3-hydroxybutyrate-co-3-hydroxyvalerate) Microfilled Anhydride-Modified Crude Lignin Blend Biodegradable Materials," *International Journal of Biological Macromolecules* 304 (2025): 140985, https://doi.org/10.1016/j.ijbiomac.2025.140985.

33. S. Lawless, B. Laycock, P. Lant, and S. Pratt, "Solvent-Based Synthesis, Structural Elucidation and Thermal Characterisation of Free Radical Grafted PHBV," *Polymer Degradation and Stability* 229 (2024): 110976, https://doi.org/10.1016/j.polymdegradstab.2024.110976.

34. X. Han, Y. Han, Y. Jin, et al., "Microcrystalline Cellulose Grafted Hyperbranched Polyester With Roll Comb Structure for Synergistic Toughening and Strengthening of Microbial PHBV/Bio-Based Polyester Elastomer Composites," *International Journal of Biological Macromolecules* 242 (2023): 124608, https://doi.org/10.1016/j.ijbiomac.2023.124608.

35. J. M. Maita, S. Rommel, J. R. Davis, et al., "Grain Size Effect on the Mechanical Properties of Nanocrystalline Magnesium Aluminate Spinel," *Acta Materialia* 251 (2023): 118881, https://doi.org/10.1016/j.actamat.2023.118881.

36. K. Liu, F. Liu, W. Zhang, et al., "Design and Development of Outstanding Strain Properties in NBT-Based Lead-Free Piezoelectric Multilayer Actuators by Grain-Orientation Engineering," *Acta Materialia* 246 (2023): 118696, https://doi.org/10.1016/j.actamat.2023.118696.

37. S.-D. Baek, W. Shao, W. Feng, et al., "Grain Engineering for Efficient Near-Infrared Perovskite Light-Emitting Diodes," *Nature Communications* 15, no. 1 (2024): 10760.

38. S. Wang, S. Frisch, H. Zhang, et al., "Grain Engineering for Improved Charge Carrier Transport in 2D Lead-Free Perovskite Field-Effect Transistors," *Mater Horiz* 9, no. 10 (2022): 2633–2643.

39. Q. Chai, F. Zhang, Q. Zhou, et al., "Superior Energy Storage Properties and Optical Transparency in $K_{0.5}$ $Na_{0.5}$ NbO_3 -Based Dielectric Ceramics via Multiple Synergistic Strategies," *Small* 19, no. 19 (2023): 2207464, https://doi.org/10.1002/smll.202207464.

40. Z. Zhu, A. Bashir, X. Wu, et al., "Highly Integrated Phase Change and Radiative Cooling Fiber Membrane for Adaptive Personal Thermal Regulation," *Advanced Functional Materials* 35, no. 9 (2025): 2416111.

41. J. S. C. Lo, X. Chen, S. Chen, et al., "Fabrication of Multilayer Superhydrophobic and Biodegradable Filters Through Electrospinning and Electrospraying of PHA-SiO2 Biopolymer Composites," *Chemical Engineering Journal* 512 (2025): 162466, https://doi.org/10.1016/j.cej.2025.162466.

42. J. E. Karbowniczek, K. Berniak, J. Knapczyk-Korczak, et al., "Strategies of Nanoparticles Integration in Polymer Fibers to Achieve Antibacterial Effect and Enhance Cell Proliferation With Collagen Production in Tissue Engineering Scaffolds," *Journal of Colloid and Interface Science* 650: 1371–1381, https://doi.org/10.1016/j.jcis.2023.07.066.

43. R. M. Michell and A. J. Müller, "Confined Crystallization of Polymeric Materials," *Progress in Polymer Science* 54 (2016): 183–213, https://doi.org/10.1016/j.progpolymsci.2015.10.007.

44. T. Kongkhlang, K. Tashiro, M. Kotaki, and S. Chirachanchai, "Electrospinning as a New Technique to Control the Crystal Morphology and Molecular Orientation of Polyoxymethylene Nanofibers," *Journal of the American Chemical Society* 130, no. 46 (2008): 15460–15466, https://doi.org/10.1021/ja804185s.

45. C. Su, G. Shi, X. Li, et al., "Uniaxial and Mixed Orientations of Poly (Ethylene Oxide) in Nanoporous Alumina Studied by X-Ray Pole Figure Analysis," *Macromolecules* 51, no. 23 (2018): 9484–9493, https://doi.org/10.1021/acs.macromol.8b01801.

46. H. Shao, D. Niu, B. Liu, et al., "Mono-Layer Films With Superior Barrier Properties and Full Recyclability: The System of Poly(ethylene terephthalate) /Poly(glycolic acid)," *Polymer* 265 (2023): 125594, https://doi.org/10.1016/j.polymer.2022.125594.

16136829, 2026, 14, Downloaded from https://onlinelibrary.wiley.com/doi/10.1002/smll.202509404 by Jilin University, Wiley Online Library on [07/11/2026]. See the Terms and Conditions (https://onlinelibrary.wiley.com/terms-and-conditions) on Wiley Online Library for rules of use; OA articles are governed by the applicable Creative Commons License

47. P. Li, Y. Huang, L. Lan, D. Xu, Y. Dan, and L. Jiang, "UV/Blue-Light-Blocking Polylactide Films Derived From Bio-Sources for Food Packaging Application," *International Journal of Biological Macromolecules* 306 (2025): 141751, https://doi.org/10.1016/j.ijbiomac.2025.141751.

48. J. Li, Q. Ban, M. Xu, et al., "Tissue-Adhesive, Silk-Based Conductive Hydrogel With High Stretchable, Transparent, Healable and Degradable Properties for Real-Time, Precise Monitoring of Tissue Motions and Electrocardiogram Under Sweaty Condition," *Journal of Colloid and Interface Science* 691 (2025): 137455, https://doi.org/10.1016/j.jcis.2025.137455.

49. Y. Lu, X. Xiao, Y. Zhan, et al., "Functional Transparent Nanocomposite Film With Thermochromic and Hydrophobic Properties Fabricated by Electrospinning and Hot-Pressing Approach," *Ceramics International* 44, no. 1 (2018): 1013–1018, https://doi.org/10.1016/j.ceramint.2017.10.037.

50. W. Shi and Z. Chen, "Mechanical, Rheological, and Crystallinity Properties of Polylactic Acid/Polyethylene Glycol-Polydimethylsiloxane Copolymer Blends by Melt Blending," *Journal of Applied Polymer Science* 140, no. 4 (2023): 53346.

51. D. Li, Y. Li, Y. Zhang, Y. Xu, X. Zhang, and M. Hakkarainen, "Designing Biobased Poly(ethylene-co-isosorbide terephthalate) Copolyesters With Tunable Properties and Degradability," *Biomacromolecules* 26, no. 4 (2025): 2304–2316.

52. X. Zhong, R. Li, Z. Wang, Y. Wang, W. Wang, and D. Yu, "Highly Flexible, Transparent Film Prepared by Upcycle of Wasted Jute Fabrics With Functional Properties," *Process Safety and Environmental Protection* 146 (2021): 718–725.

53. P. Wang, J. Song, J. Wu, et al., "Lignosulfonates Enable the Coproduction of Fibrillated Lignocellulose and Fermentable Sugars From Chemi-Thermomechanical Wood Fibers," *ACS Sustainable Chem Eng* 12, no. 18 (2024): 7170–7178.

54. T. Qiang, W. Ren, and L. Chen, "Biodegradable, High Mechanical Strength, and Eco-Friendly Pectin-Based Plastic Film," *Food Hydrocolloids* 149 (2024): 109539, https://doi.org/10.1016/j.foodhyd.2023.109539.

55. W. Ma, Y. Lu, Y. Liu, D. Li, and L. Li, "Enhanced Permeability of ZnO/PE Films by Stretching and Its Application in Pakchoi Preservation," *Food Packaging and Shelf Life* 43 (2024): 101296, https://doi.org/10.1016/j.fpsl.2024.101296.

56. Y. Xie, S. Y. H. Abdalkarim, Z. Ji, Z. Chen, M. Wang, and H.-Y. Yu, "Various-Sized Nanocelluloses Induced Stereocomplexes Crystallization Formation and Its Mechanism of Stereoisomers Poly(lactide acid) Blend," *ACS Sustainable Chem Eng* 11, no. 35 (2023): 13164–13178.

57. X. Han, Y. Han, Y. Jin, et al., "Tailoring Compatibility and Toughness of Microbial Poly(3-hydroxybutyrate-co-3-hydroxyvalerate)/Bio-Based Polyester Elastomer Blends by Epoxy-Terminated Hyperbranched Polyester," *International Journal of Biological Macromolecules* 220 (2022): 1163–1176, https://doi.org/10.1016/j.ijbiomac.2022.08.130.

58. E. C. Quinn, A. H. Westlie, A. Sangroniz, and E. Y.-X. Chen, "Installing Controlled Stereo-Defects Yields Semicrystalline and Biodegradable Poly(3-hydroxybutyrate) With High Toughness and Optical Clarity," *Journal of the American Chemical Society* 145, no. 10 (2023): 5795–5802.

59. H. Chen, C. Su, G. Shi, X. Li, X. Zhang, G. Liu, and D. Wang, "Deformation Mechanism of Poly(3-alkylthiophene) Studied by in Situ X-Ray Scattering and Texture Analysis," *Macromolecules* 51, no. 20 (2018): 8306–8315, https://doi.org/10.1021/acs.macromol.8b01223.

60. T. Iwata, M. Fujita, Y. Aoyagi, Y. Doi, and T. Fujisawa, "Time-Resolved X-ray Diffraction Study on Poly[(R)-3-hydroxybutyrate] Films During Two-Step-Drawing: Generation Mechanism of Planar Zigzag Structure," *Biomacromolecules* 6, no. 3 (2005): 1803–1809, https://doi.org/10.1021/bm050152s.

61. K. Patel, A. Patel, V. P. Jethwa, H. Patel, and G. K. Solanki, "X-ray Diffraction Analysis of Orthorhombic SnSe Nanoparticles by Williamson–Hall, Halder–Wagner and Size–Strain Plot Methods," *Chemical Physics Impact* 8 (2024): 100547, https://doi.org/10.1016/j.chphi.2024.100547.

62. Y. Lim, J. Jin, and B. Bae, "Optically Transparent Multiscale Composite Films for Flexible and Wearable Electronics," *Advanced Materials* 32, no. 35 (2020): 1907143, https://doi.org/10.1002/adma.201907143.

63. K. Klier, "Absorption and Scattering in Plane Parallel Turbid Media," *Journal of the Optical Society of America* 62, no. 7 (1972): 882, https://doi.org/10.1364/JOSA.62.000882.

64. H. Zhu, S. Parvinian, C. Preston, O. Vaaland, Z. Ruan, and L. Hu, "Transparent Nanopaper With Tailored Optical Properties," *Nanoscale* 5, no. 9 (2013): 3787.

65. C. Tang and H. Liu, "Cellulose Nanofiber Reinforced Poly(vinyl alcohol) Composite Film With High Visible Light Transmittance," *Composites Part A: Applied Science and Manufacturing* 39, no. 10 (2008): 1638–1643, https://doi.org/10.1016/j.compositesa.2008.07.005.

66. J. Yang, L. Chang, X. Zhang, Z. Cao, and L. Jiang, "Ionic Liquid-Enhanced Assembly of Nanomaterials for Highly Stable Flexible Transparent Electrodes," *Nano-Micro Letter* 16, no. 1 (2024): 140.

67. P. Escobedo, C. E. Ramos-Lorente, A. Martínez-Olmos, et al., "Wireless Wearable Wristband for Continuous Sweat pH Monitoring," *Sensor Actuat B-Chem* 327 (2021): 128948.

Supporting Information

Additional supporting information can be found online in the Supporting Information section.

Supporting File: smll72344-sup-0001-SuppMat.docx

16136829, 2026, 14, Downloaded from https://onlinelibrary.wiley.com/doi/10.1002/smll.202509404 by Jilin University, Wiley Online Library on [07/11/2026]. See the Terms and Conditions (https://onlinelibrary.wiley.com/terms-and-conditions) on Wiley Online Library for rules of use; OA articles are governed by the applicable Creative Commons License